

Absorbing phase transitions in granular suspensions

Part III Project Report



UNIVERSITY OF
CAMBRIDGE
Department of Physics

Candidate number: 8255S

Supervisor: Dr. Christopher Ness

Date: 12th May 2018

Abstract

In this work, absorbing state phase transitions in athermal granular suspensions sheared at low Reynolds number are explored using numerical simulations. The system is only able to self-organise into an absorbing state if the strain amplitude is below a critical value γ_c , which is strongly dependent on concentration. Two considerably different types of absorbing states are observed at concentrations above and below the critical jamming volume fraction (ϕ_c). At low concentrations, hydrodynamics dominates and the equations of motion are time-reversible, offering a clear route to reversibility. At high concentrations, contact forces dominate and the equations of motion are irreversible. However, at low strain amplitudes, the particles are able to self-organise towards an absorbing state. Microscopic and macroscopic reversibility are considered in an attempt to characterise the transition, and a phase diagram indicating regions in which both types of reversibility are satisfied is constructed. A critical volume fraction at which absorbing states cannot be formed, even for infinitesimally small strain amplitudes, is identified as the jamming point and estimated to be $\phi_c = 0.650 \pm 0.004$. Good agreement is found between microscopic and macroscopic reversibility criteria for suspensions at concentrations below the jamming point, but inconsistency at concentrations above the jamming point prevents unification of both types of absorbing-state transitions.

Contents

1	Introduction	2
2	Models & Methods	5
2.1	Numerical Model for Simulations	5
2.2	Implementing the model	6
2.3	Simulation procedure	8
2.4	Identifying Absorbing States	9
3	Results & Discussion	10
3.1	Microscopic reversibility	10
3.2	Active particles	11
3.3	Macroscopic reversibility	13
3.4	Phase diagram	15
3.5	Hyperuniformity	17
4	Conclusions	17
	Appendix A Scalar resistances	19
	Appendix B Repeated simulations	19

1 Introduction

Absorbing-state phase transitions are thought to be one of the few fundamentally non-equilibrium phenomena with no equivalent in equilibrium systems. They are closely related to directed percolation and there are a wide range of applications, including catalytic reactions, flow through porous materials and the spreading of forest fires or epidemics [1]. Recently, there has been significant interest in self-organised criticality (SOC) and the emergence of absorbing states in suspensions under oscillatory shear at low Reynolds number, when inertia is negligible compared to viscous forces. Such suspensions of athermal particles are perhaps the simplest class of experimental systems in which these phase transitions can be observed and quantified. They are also of interest in their own right as a widespread material used in industry and nature, so understanding their behaviour and being able to reliably predict flow properties is important [2]. However, characterising their statistical and rheological properties remains a fundamental challenge to physicists and engineers.

For dilute concentrations, where the volume of suspended particles is negligible compared to the volume of the material at-large, the system is governed by the reversible Stokes equations of motion, and reversing the direction of shear is equivalent to reversing time. It has been shown [3, 4, 5] that, under the right conditions, the system self-organises towards a critical point and undergoes a dynamical phase transition from a fluctuating steady state to an absorbing state. Once the absorbing state is entered, flows become time-reversible, so particles retrace their trajectories when the direction of shear is reversed. The system becomes ‘trapped’ in the absorbing state and is unable to transition to a different state. The phase transition is a non-equilibrium process, so detailed balance and time-reversibility are violated at the transition point.

At intermediate concentrations, particles collide with each other and experience irreversible contact forces. In this regime, the strain amplitude is crucial, since larger deformations are more likely to bring particles into contact, preventing reversibility. The system generally remains in a fluctuating diffusive state – in athermal conditions, diffusion is activated by the applied deformation rather than thermal fluctuations. However, irreversible collisions allow the system to explore a greater fraction of configuration space and can cause particles to self-organise to avoid future collisions [4]. Self-organisation can lead to a phase transition to an absorbing state, in which particles no longer come into close contact and therefore return to their original positions after each shear cycle. The system then maintains configurational invariance under further oscillation.

Cort   *et al.* used numerical simulations to model a simple two-dimensional suspension under oscillatory shear for different strain amplitudes [4]. They defined particles to be ‘active’ if they collide with another particle in a given shear cycle. Below a critical strain amplitude (γ_c), the fraction of active particles f_a decays to zero

eventually, indicating the system has reached an absorbing state (**Fig. 1**). Above γ_c , however, the system reaches a steady state where a finite non-zero fraction of particles always remains active and f_a fluctuates about a steady-state value f_a^∞ . When these active particles collide, their trajectories are altered irreversibly. This may bring them into contact with previously inactive particles, causing them to become active. Hence, an absorbing state cannot be formed if f_a^∞ is non-zero. They also found that the characteristic time to reach a steady state diverges with an exponential power law as γ_c is approached.

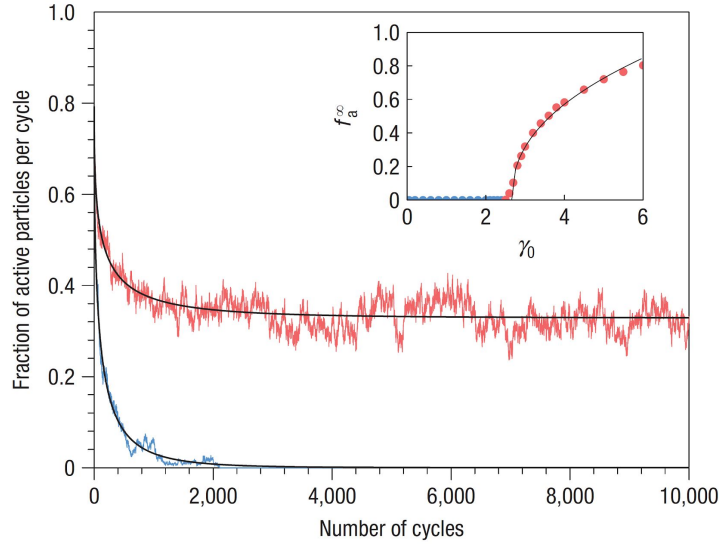


Figure 1: Fig. 2c from Corté *et al.* 2008 [4]. Fraction of active particles f_a as a function of number of shear cycles for two different strain amplitudes above (red) and below (blue) the critical shear amplitude (γ_c). Inset: The steady-state fraction of active particles (f_a^∞) as a function of strain amplitude (γ_0). The blue and red data points correspond to data below and above γ_c , respectively.

It has been shown that the threshold for irreversibility is strongly affected by the concentration for both experimental data [3, 4, 5] and numerical simulations [3, 4]. As the concentration is increased, the critical strain amplitude decreases substantially.

If the density is increased to the critical volume fraction (ϕ_c), also referred to as the jamming point, the system undergoes a jamming phase transition [6], where overcrowding of particles causes the dynamics to become arrested and the material behaves like a solid. Beyond this point, inter-particle contact forces, rather than hydrodynamics, become dominant. Despite the irreversible nature of such forces, precisely reversible flows have been reported [7]. In this case, ‘coarse-grained’ reversibility arises due to balancing of repulsive forces on caged particles, rather than due to the equations of motion themselves being reversible. The system self-organises into a limit-cycle absorbing state and particles return to the same position each shear cycle (**Fig. 2**).

In this project, the behaviour of dense granular suspensions is explored using numerical simulations. The

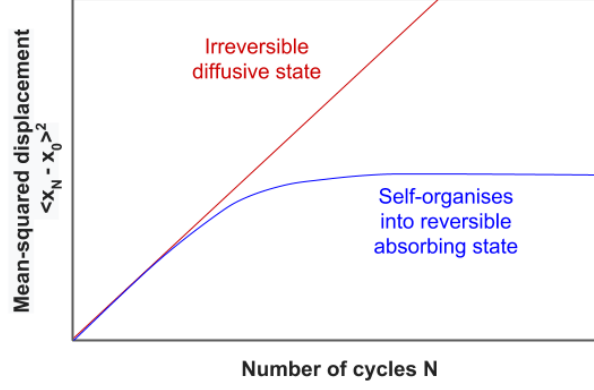


Figure 2: Sketch of the mean-squared displacement after N cycles from the initial particle positions for an irreversible diffusive state (red) and a system that self-organises to form a reversible absorbing state (blue).

primary aim is to explore the emergence of absorbing states in periodically sheared suspensions over a wide range of concentrations spanning the jamming point, and to produce a phase diagram similar to the initial estimate shown in **Fig. 3**. This is based on evidence that absorbing transitions occur above [3, 4, 5] and below [7] the jamming point, but, since they are due to different mechanisms, it is not clear what happens at the jamming point itself.

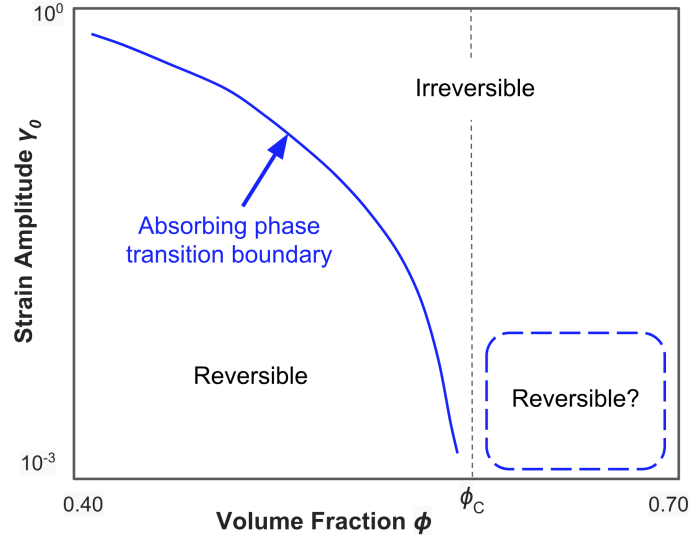


Figure 3: Sketch of the expected phase diagram with reversible and irreversible states, where the blue line indicates the absorbing phase transition boundary. We expect to find a second reversible state at high density close to the marked region beyond the critical jamming volume fraction (ϕ_c). The values on axes are simply approximate guidelines for the ranges involved.

The relevant theoretical background and methods used are described in Section 2. In Section 3, the results are presented and discussed in detail, before the major findings and conclusions are summarised in Section 4.

2 Models & Methods

2.1 Numerical Model for Simulations

The numerical simulations performed in this project consider athermal, neutrally buoyant particles using the same model outlined in Ref. [8]. Solid particles in suspension experience inertial forces, contact forces from pair interactions, hydrodynamic viscous drag forces from the fluid and lubrication forces due to movement of two particles past each other in close contact. Hydrodynamic interactions between particles are modelled using the resistance matrix formalism described by Ball & Melrose for identical spheres [9], but forces and torques are calculated from the equations given by Jeffrey for unequal spheres [10].

The model is constructed from frame-invariant pairwise interactions and the average fluid flow field is assumed to be the same as the average particle velocity field. For sufficiently concentrated suspensions, the dominant terms for short range interactions are the lubrication forces from nearest neighbours, given by the scalar resistance matrix elements X_A^{11} , Y_A^{11} , Y_B^{11} , Y_B^{21} , Y_C^{11} and Y_C^{12} (full expressions are given in Appendix A).

Consider two particles with centres at positions \mathbf{x}_1 , \mathbf{x}_2 and radii a_1 , a_2 , suspended in a fluid with shear viscosity η_f . The particle surfaces are separated by a gap size $h = |\mathbf{r}| - (a_1 + a_2)$, where $\mathbf{r} = \mathbf{x}_2 - \mathbf{x}_1$ is the centre-centre separation vector. Defining a non-dimensional quantity $\xi = 2h/(a_1 + a_2)$, it follows [11] that the scalar resistances diverge as $1/\xi$ and $\ln(1/\xi)$ to leading order, so interactions with $h > 0.05a$ (where a is the smaller particle radius) are neglected. If the particles are moving with velocities \mathbf{U}_1 , \mathbf{U}_2 and rotating with angular velocities $\mathbf{\Omega}_1$, $\mathbf{\Omega}_2$, the force \mathbf{F}^h and torque $\mathbf{\Gamma}^h$ acting on particle 1 can be shown [12] to be:

$$\mathbf{F}^h/\eta_f = (X_A^{11}\mathbf{n} \otimes \mathbf{n} + Y_A^{11}(\mathbf{I} - \mathbf{n} \otimes \mathbf{n})) \cdot (\mathbf{U}_2 - \mathbf{U}_1) + Y_B^{11}(\mathbf{\Omega}_1 \times \mathbf{n}) + Y_B^{21}(\mathbf{\Omega}_2 \times \mathbf{n}) \quad (1)$$

$$\mathbf{\Gamma}^h/\eta_f = Y_B^{11}(\mathbf{U}_2 - \mathbf{U}_1) \times \mathbf{n} - (\mathbf{I} - \mathbf{n} \otimes \mathbf{n}) \cdot (Y_C^{11}\mathbf{\Omega}_1 + Y_C^{12}\mathbf{\Omega}_2) \quad (2)$$

where $\mathbf{n} = \mathbf{r}/|\mathbf{r}|$ is the centre-centre unit vector. The hydrodynamic stresslet contribution for particle 1 resulting from its pairwise interaction with particle 2 is therefore $\mathbf{S}^h = -\frac{1}{2}(\mathbf{F}^h\mathbf{r}^T + (\mathbf{F}^h)^T\mathbf{r})$.

To avoid diverging forces, the lubrication forces are regularised for particles separated by less than a minimum gap size $h_{min} = 10^{-3}a$. This is based on experimental evidence that lubrication layers break down in suspensions under large stress [13]. Particles also experience a repulsive contact force if they come into mechanical contact i.e. if the separation of their centres is less than the sum of their radii, so they overlap. Once a contact is initiated, the tangential displacement of each particle \mathbf{u} accumulates until the contact is broken, at which point it is reset. For two particles with contact overlap $\delta = ((a_1 + a_2) - |\mathbf{r}|)\Theta((a_1 + a_2) - |\mathbf{r}|)$, the force and torque

on the first particle are calculated as [14]:

$$\mathbf{F}^c = k_n \delta \mathbf{n} - k_t \mathbf{u} \quad (3)$$

$$\mathbf{\Gamma}^c = a_1 k_t (\mathbf{n} \times \mathbf{u}) \quad (4)$$

where k_n and k_t are stiffness constants for normal and tangential components respectively and $k_t/k_n = 2/7$. The tangential component is restricted to values $|k_t \mathbf{u}| \leq \mu k_n \delta$, where μ is the Coulomb coefficient of friction; if $|k_t \mathbf{u}|$ exceeds this limit, a sliding contact regime is entered. The contact force stresslet is given by $\mathbf{S}^c = -\mathbf{F}^c \mathbf{r}^T$.

The rate of strain particles experience is controlled by a velocity gradient tensor \mathbf{U}^∞ with components $\partial v_i / \partial x_j$. This can be separated into symmetric and antisymmetric parts \mathbf{E}^∞ and $\mathbf{\Omega}^\infty$, corresponding to extensional and rotational deformations, respectively. The background flow of the suspending fluid at position \mathbf{x} can therefore be written as $\mathbf{U}^\infty(\mathbf{x}) = \mathbf{E}^\infty \mathbf{x} + \mathbf{\Omega}^\infty \times \mathbf{x}$, and the drag force and torque experienced by particle 1 are given by:

$$\mathbf{F}^d = -6\pi\eta_f a_1 (\mathbf{U}_1 - \mathbf{U}^\infty(\mathbf{x}_1)) \quad (5)$$

$$\mathbf{\Gamma}^d = -8\pi\eta_f a_1^3 (\mathbf{\Omega}_1 - \mathbf{\Omega}^\infty(\mathbf{x}_1)) \quad (6)$$

The drag force stresslet for each particle is $\mathbf{S}^d = -(20\pi/3)\eta_f a_1^3 \mathbf{E}^\infty$.

Hydrodynamic stresslets are summed over all hydrodynamically interacting pairs p_h , contact stresslets are summed over pairs in close contact p_c and drag stresslets are summed over individual particles i . This allows the overall stress tensor $\boldsymbol{\sigma}$ to be calculated by summing over all contributions as follows:

$$\boldsymbol{\sigma} = -2\eta_f \mathbf{E}^\infty + (1/V) \left(\sum_{p_h} \mathbf{S}^h + \sum_{p_c} \mathbf{S}^c + \sum_i \mathbf{S}^d \right) \quad (7)$$

The relative magnitudes of the hydrodynamic and contact stresses depend on the accumulated strain. For concentrations below the jamming point, the contributions to relative viscosity η/η_f from hydrodynamic and contact forces take the form shown in **Fig. 4**. Hydrodynamic stress dominates at small strains, but as the strain increases, particles are able to form mechanical contacts and the contact stress increases until it exceeds hydrodynamic stress.

2.2 Implementing the model

The model described above is implemented in the molecular dynamics package LAMMPS [15]. Simulations performed comprise a mixture of 2,500 unequal solid spherical particles suspended in a fluid and an aspect ratio

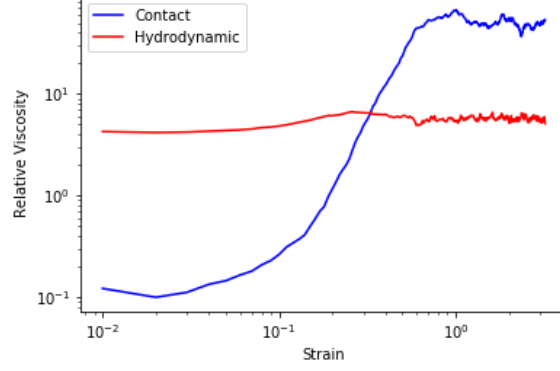


Figure 4: Data from a numerical simulation of a suspension subject to a linearly increasing strain γ . The contributions to relative viscosity (η/η_f) from contact stress (blue) and hydrodynamic stress (red) are shown, where the viscosity of the particle suspension is $\eta = \sigma/\dot{\gamma}$.

of 1 : 1.4 is used, with equal numbers of each size. Particles are randomly placed in the simulation box and the initial system configuration is allowed to evolve freely for a sufficiently long time to ensure a steady state with minimal particle-particle contacts is reached before any shearing occurs. The simulation box dimensions are chosen in each case to give the desired volume fraction of particles.

A simple oscillatory strain $\gamma(t) = \gamma_0 \sin(\omega t)$, with amplitude γ_0 and frequency ω , is applied to the system. This is achieved by deforming the triclinic simulation box of length L_{box} – the tilt length $\Delta L_{xz}(t) = L_{\text{box}}\gamma(t)$ is varied sinusoidally in time (**Fig. 5**). If a particle crosses a periodic boundary, its velocity is remapped according to the velocity gradient across the box, perpendicular to that boundary. If the tilt length exceeds half the box length ($\Delta L_{xz} > L_{\text{box}}/2$), the particle coordinates are remapped; this allows arbitrarily large shear deformations to be performed without the box becoming highly skewed, such that force calculations become computationally expensive.

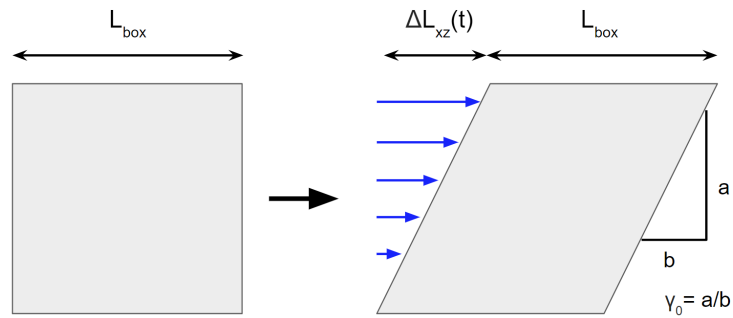


Figure 5: Cartoon illustrating how a simple oscillatory shear strain with amplitude γ_0 is applied to the system. The simulation box is deformed by varying the tilt length $\Delta L_{xz}(t)$ sinusoidally in time.

The behaviour of the system is controlled by three dimensionless quantities: the volume fraction (ϕ), the Stokes number (St) and the scaled shear rate ($\hat{\gamma}$). The volume fraction, also referred to as the concentration, is varied throughout. The Stokes number $St = \tau_p/\tau_f$ is the ratio of the relaxation time of the particle (τ_p)

to the relaxation time of the surrounding fluid (τ_f). For low Reynolds number flow, this can be written as $St = 2\rho\dot{\gamma}a^2/9\eta_f$, where ρ is the particle density. The Stokes number is kept small ($St \ll 1$) to ensure particles follow fluid streamlines closely and inertia is small compared to viscous forces. The scaled shear rate $\hat{\gamma} = 2\dot{\gamma}a/\sqrt{k_n/(2\rho a)}$ determines particle softness [16]. It is kept small throughout, which means the particles are very hard, approximating experimental conditions.

LAMMPS sums the forces acting on each particle i and computes the inertia from the following equation of motion:

$$m_i\ddot{\mathbf{r}}_i = \mathbf{F}_i^h + \mathbf{F}_i^c + \mathbf{F}_i^d \quad (8)$$

There is no thermal motion, but despite ensuring $St \ll 1$, it is possible for particles to have non-zero inertia. Strictly zero inertia models do exist, but they are extremely computationally expensive; this model was therefore opted for as a practicable compromise. The equation of motion is discretised and integrated using a Velocity-Verlet algorithm, allowing particle trajectories to be updated. LAMMPS uses Verlet and cell lists to track nearest neighbours and reduce computation time.

2.3 Simulation procedure

For each volume fraction, simulations were performed over a range of strain amplitudes ($10^{-4} \leq \gamma_0 \leq 10^1$). A small number of approximately evenly spaced (in log-space) amplitudes were initially sampled, before focusing on the vicinity of the absorbing transition. The individual components of stress were recorded at regular intervals, as well as the particle coordinates at the start of each shear cycle, allowing the cycle displacement to be calculated.

The distance a given particle has moved at the end of the n th shear cycle from its position at the start of that shear cycle can be computed and used to define the cycle displacement $\Delta x_c(n) = |\mathbf{x}(n) - \mathbf{x}(n-1)|$. Averaging across all particles gives the root mean square (RMS) cycle displacement $\Delta x_c^{\text{rms}}(n) = \sqrt{\langle \Delta x_c^2(n) \rangle}$, which is analogous to an instantaneous diffusion coefficient $D(n)$, defined over a time scale equal to the shear cycle period $T = 2\pi/\omega$. In three dimensions, $\langle \Delta x_c^2(n) \rangle \equiv 6D(n)T$, so the diffusion coefficient can be written as $D(n) = \omega \langle \Delta x_c^2(n) \rangle / 12\pi$. Simulations were extended until the system reached a steady state i.e. when Δx_c^{rms} reaches a plateau (**Fig. 6**), before any measurements were made. The steady-state cycle displacement Δx_c^∞ was then calculated by averaging over the final three shear cycles.

The xz-component of the stress tensor, referred to as σ , was calculated from its individual contributions using equation 7, while the strain is already known from the applied shear.

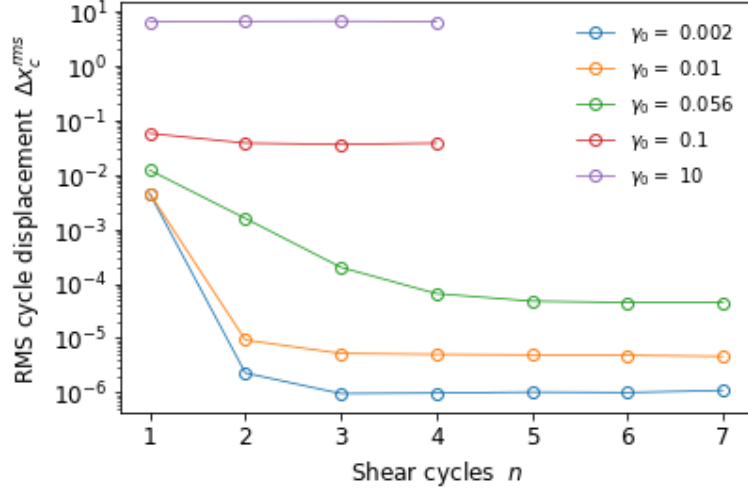


Figure 6: Volume fraction $\phi = 0.62$. The RMS cycle displacement Δx_c^{rms} evolution as a function of the number of shear cycles n for a range of different strain amplitudes (γ_0).

2.4 Identifying Absorbing States

The ways in which absorbing states can be identified fall into two broad categories. Macroscopic reversibility focuses on large scale properties of the system as a whole, while microscopic reversibility analyses the motion of individual particles.

Macroscopic reversibility can be explored by considering the relationship between stress and strain. For periodic shear at frequency ω , the phase difference $\delta = \omega\tau$ between stress and strain can be determined once the lag time τ has been computed by taking their cross correlation. It is then instructive to calculate the storage (G') and loss (G'') moduli as follows:

$$G' = \frac{\sigma_0}{\gamma_0} \cos(\delta) \quad G'' = \frac{\sigma_0}{\gamma_0} \sin(\delta) \quad (9)$$

where σ_0 and γ_0 are the stress and strain amplitudes, respectively.

For low concentration absorbing states, hydrodynamic forces dominate; in an ideal case, the force is purely viscous and the stress is proportional to strain rate. The stress and strain oscillate in quadrature ($\delta = \pi/2$), with a characteristic circular Lissajous curve (**Fig. 7a**). The storage modulus is negligible and almost all energy is dissipated by viscous forces.

For high concentration absorbing states, contact forces dominate. Contact forces are purely elastic, so stress is proportional to strain and they oscillate in phase ($\delta = 0$), with a linear Lissajous curve (**Fig. 7b**). The loss modulus is negligible and almost all energy is stored by elastic contact forces. The examples shown in **Fig. 7** represent ideal macroscopically reversible cases – if neither G' or G'' is negligible, the system is classified as

macroscopically irreversible.

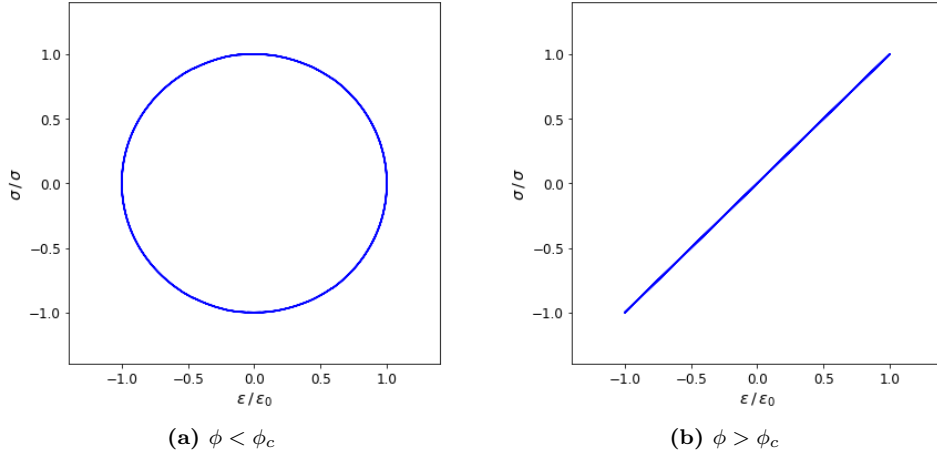


Figure 7: The stress-strain relationships for ideal absorbing states where the dominant interactions are due to (a) hydrodynamic forces ($\phi < \phi_c$) and (b) contact forces ($\phi > \phi_c$).

Investigating microscopic reversibility involves considering the trajectories of individual particles and determining whether they are reversible or not. Corté *et al.* [4] used a simple two-dimensional system, where particles only interact if they come into physical contact, and therefore they could easily check if a collision had occurred. In the simulations performed in this project, recording particle positions and checking whether a collision occurs for every single time step is both computationally demanding and produces excessively large data files. It is easier merely to record the positions of particles at the start of every shear cycle and calculate the cycle displacement. Particles moving along reversible trajectories do not collide with other particles and return to the same position at the end of each shear cycle ($\Delta x_c \approx 0$). However, particles interact with each other and the surrounding fluid through long range interactions, so it is not possible to have truly inactive particles. Instead, for the purposes of this analysis, they considered to be moving along reversible trajectories if their cycle displacement $\Delta x_c \leq 10^{-5}a$. This is somewhat arbitrary, but is the same approach taken in Ref. [17] and small changes to this criteria are not expected to affect the qualitative findings.

3 Results & Discussion

3.1 Microscopic reversibility

A typical example of the form of Δx_c^∞ as a function of γ_0 for volume fractions below the jamming point is shown in **Fig. 8a**. For small strain amplitudes, $\Delta x_c^\infty \ll \gamma_0$ and the slope is close to unity, implying a linear relationship between cycle displacement and strain amplitude. Despite ensuring that the Stoke's number was kept small, this linear relationship is indicative of inertial effects. At a particular point, defined as the microscopic critical

strain amplitude (γ_c^{micro}), the slope begins to increase much more sharply and the cycle displacement increases such that $\Delta x_c^\infty \sim \gamma_0$. This suggests a fundamental change in the behaviour of the system, interpreted as the transition from a reversible absorbing state to an irreversible fluctuating state. Approaching the jamming transition, the inertial regime is restricted to lower γ_0 .

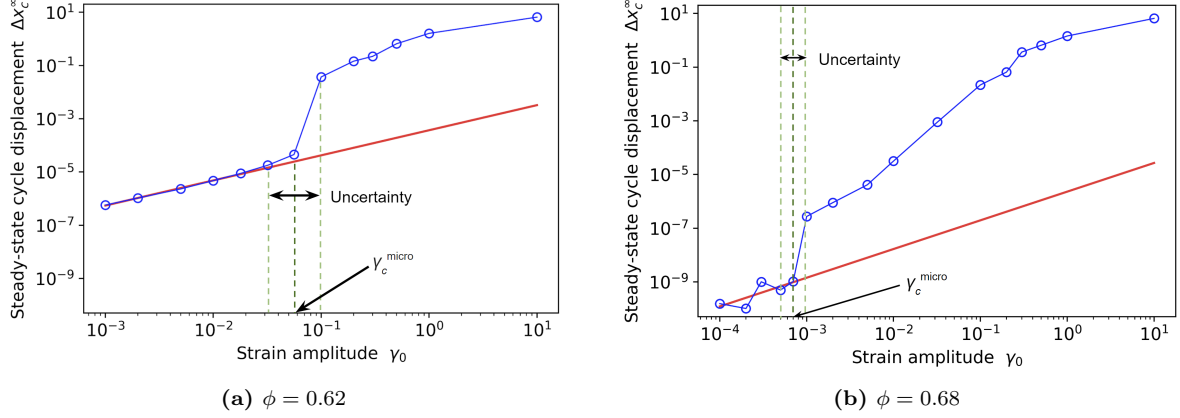


Figure 8: The steady-state cycle displacement Δx_c^∞ as a function of strain amplitude (γ_0) for typical suspensions with concentration **(a)** below the jamming point ($\phi = 0.62$) and **(b)** above the jamming point ($\phi = 0.68$). In each case, the microscopic critical strain amplitude (γ_c^{micro}), at which the absorbing-state phase transition occurs, is indicated, along with the corresponding uncertainty.

A typical example for concentrations beyond the jamming transition is shown in **Fig. 8b**. Similar to low concentrations, at low strain amplitudes, $\Delta x_c^\infty \ll \gamma_0$. Unlike lower concentrations however, inertia is now due to a mixture of hydrodynamics and contact relaxation, so the slope is not necessarily unity. The slope is initially small, before sharply increasing at γ_c^{micro} . This suggests that the system is able to self-organise into an absorbing state for $\phi > \phi_c$, in agreement with Ref. [7]. As the concentration is increased, γ_c^{micro} increases, but remains small compared to most concentrations below the jamming point. Interestingly, Δx_c^∞ is typically several orders of magnitude lower than for absorbing states below the jamming point. This is likely because, for small γ_0 , the particles are trapped in cages consisting of their nearest neighbours. Only once γ_c is exceeded, can particles escape these cages and move past each other.

As the jamming point is approached, the time for the system to self-organise into an absorbing state diverges. This makes it difficult to explore systems very close to jamming, particularly with limited CPU time.

3.2 Active particles

The fraction of active particles decays to zero for small strain amplitudes ($\gamma_0 < \gamma_c$), indicating strong self-organisation towards absorbing states, while for large amplitudes it remains equal to one (**Fig. 9a**). This is similar to behaviour found by Cort   *et al.* [4], shown in **Fig. 1**, except the increase in f_a^∞ at the critical strain

amplitude is considerably sharper (**Fig. 9b**). This is likely due to the difference in the definitions of active particles, although the qualitative behaviour is still very similar.

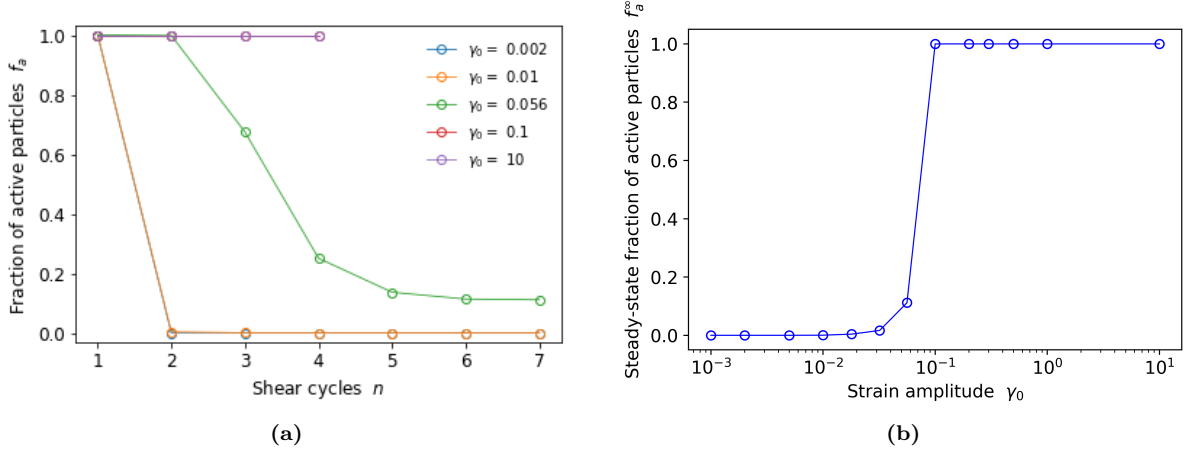


Figure 9: Volume fraction $\phi = 0.62$. **(a)** The fraction of active particles f_a as a function of the number of shear cycles n . Particles are defined as ‘active’ if their cycle displacement $\Delta x_c > 10^{-5}a$. **(b)** The steady-state fraction of active particles f_a^∞ as a function of strain amplitude (γ_0).

Interesting behaviour is observed close to the jamming point ($\phi = 0.648$) and repeated simulations were run with the same concentration to investigate further (**Fig. 10**). Changing the random seed generated different initial configurations or realisations. In realisation 2, f_a decays rapidly to zero and the system enters an absorbing state. However, in the other two realisations, f_a decreases initially, before increasing again, and the system remains in an irreversible fluctuating state. The most likely explanation is that irreversible regions of active particles are able to ‘activate’ nearby inactive regions, allowing these irreversible regions to grow. Initially, a small number of active particles interact with each other, causing them to collide with other seemingly inactive particles. These irreversible collisions change the inactive particles’ trajectories in such away that they are no longer reversible and the process repeats itself.

This demonstrates how ‘fragile’ absorbing states are; even the existence of tiny perturbations can gradually lead the system to end up far from an absorbing state. It would be interesting to see if f_a would continue to oscillate up and down until it eventually reaches zero, but unfortunately I did not have enough time to investigate this further. Ideally, each simulation should be continued for a large number of cycles after the system appears to reach a steady state.

As the jamming point is approached, absorbing states can only be formed at smaller and smaller strain amplitudes. If γ_0 is less than the minimum cycle displacement to class a particle as ‘active’, then it is likely that the system will appear to be in an absorbing state. This highlights a flaw in the somewhat arbitrary definition of active particles, which is a continuing hurdle to the characterisation of this type of phase transition.

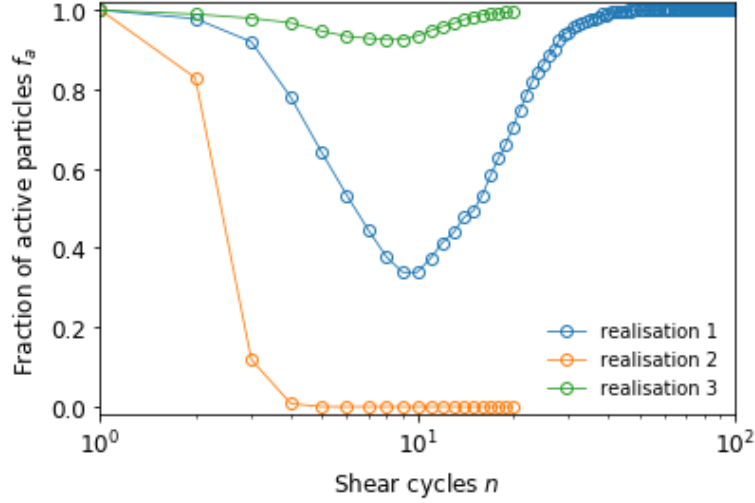


Figure 10: The fraction of active particles f_a as a function of the number of shear cycles n for system at concentration close to the jamming point ($\phi = 0.648$). Three different realisations, each generated with a different random seed are shown. Particles are defined as ‘active’ if their cycle displacement $\Delta x_c > 10^{-5}a$.

3.3 Macroscopic reversibility

The storage (G') and loss (G'') moduli were calculated using equation 9. It is apparent from **Fig. 11** that there are differences in the underlying behaviour of systems above and below the jamming transition.

Below the jamming transition ($\phi < \phi_c$), the loss modulus is greater than the storage modulus for small strain amplitudes and their ratio is fairly constant. This is as expected, since reversible hydrodynamic forces dominate. The storage modulus begins to increase and the phase angle $\tan(\delta)$ drops sharply at a particular amplitude, which is defined as the macroscopic critical strain amplitude (γ_c^{macro}). As the strain amplitude increases, the system spends more time in a high strain regime; therefore, the contribution to stress from irreversible contact forces grows, as demonstrated in **Fig. 4**. At higher strain amplitudes, G' increases sharply and $\tan(\delta)$ has a turning point, before beginning to increase. As the concentration approaches ϕ_c , there is a crossover between G' and G'' at intermediate γ_0 .

Above the jamming transition ($\phi > \phi_c$), both G' and G'' are significantly higher at all strain amplitudes because the system is ‘jammed’, and therefore the stresses involved are much greater. For low strain amplitudes, $G' \gg G''$, since elastic contact forces dominate at high concentrations. Both moduli remain fairly constant, which could be indicative of a regime in which absorbing states of the kind described in Ref. [7] exist. As the strain amplitude is increased, there is a sharp increase in G'' , followed by a drop in G' . This is similar to dynamic strain amplitude sweep tests, which are used to determine the yielding point of a linear viscoelastic material. Yielding begins at the deviation of G' from the constant linear viscoelastic regime, and the crossover of G' and G'' occurs at the onset of complete fluidisation [18].

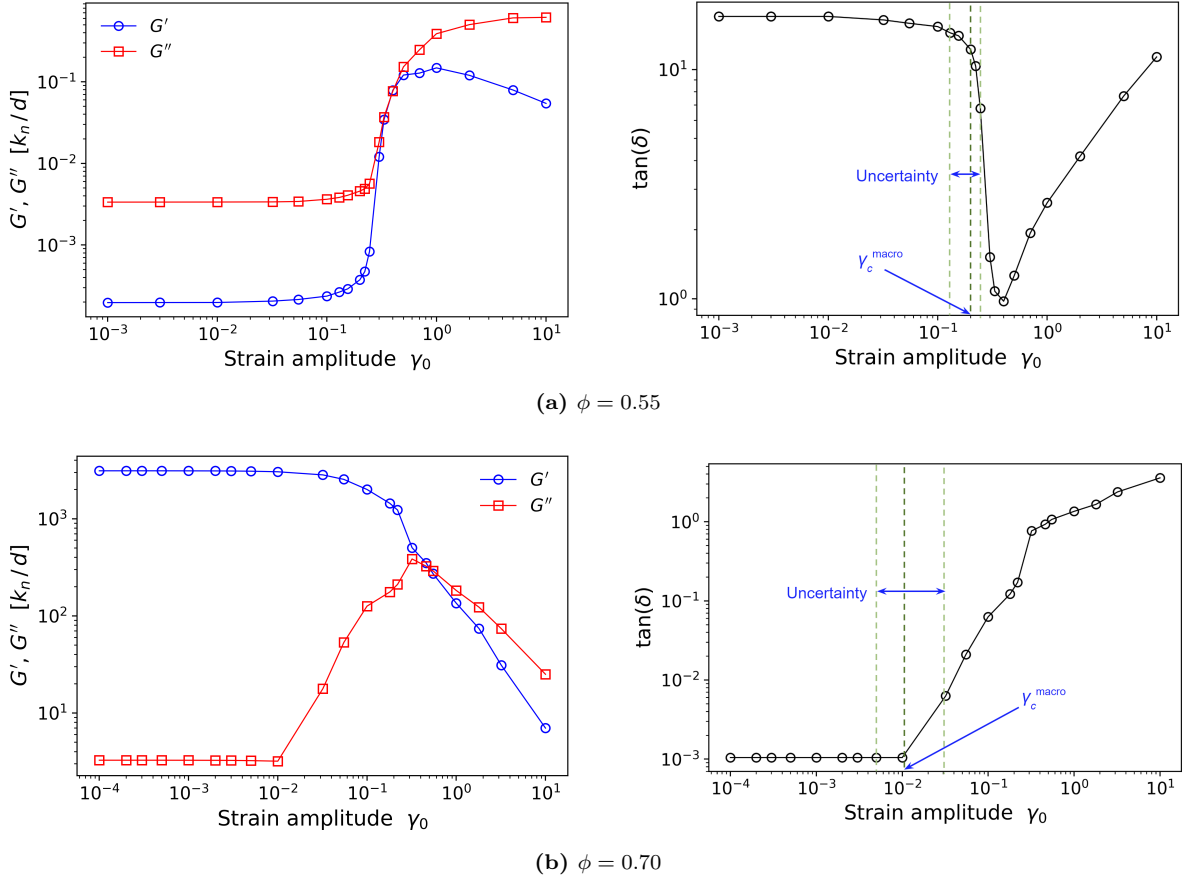


Figure 11: A typical example of storage (G') and loss (G'') moduli (left hand figures) and the phase angle $\tan(\delta)$ (right hand figures) as a function of strain amplitude (γ_0) for concentrations **(a)** below the jamming point ($\phi = 0.55$) and **(b)** above the jamming point ($\phi = 0.70$). In each case, the macroscopic critical strain amplitude at which the absorbing-state phase transition occurs is indicated (γ_c^{macro}), along with the corresponding uncertainty.

Some previous research, for example Ref. [19], focuses on the crossover of G' and G'' as the key point where a change in behaviour seen. In the simulations conducted in this work however, the system is clearly no longer in an absorbing state by the time the crossover point is reached and therefore it is not appropriate to use this point. The macroscopic critical strain amplitude (γ_c^{macro}) above the jamming transition is instead defined as the the point at which $\tan(\delta)$ begins to increase (**Fig. 11**).

For small γ_0 , the system behaves almost completely elastically, so the phase difference δ between stress and strain is very small. To ensure that data files did not become too large, the stress signal was only recorded every $\Delta t = 1,000$ ts (time steps), but this coarse-graining becomes an issue when $\delta \sim \omega \Delta t$. Due to the uncertainty in δ , this resulted in some some cases where δ was computed to be precisely zero, or even worse $\delta = -\omega \Delta t$, which is clearly unphysical. At this point, $\delta \sim 10^{-3}$, which is sufficiently small that G'' can be treated as negligible compared to G' and the system is considered to be in an absorbing state. For the purposes of plotting on logarithmic scales, I set $\delta = \omega \Delta t$ and deem deviation to be due to uncertainty from coarse-graining. These simulations could be repeated with smaller Δt to investigate this further.

Plotting normalised stress and strain further demonstrates the transition from ideal macroscopically re-

versible states, discussed in Section 2.4, to irreversible fluctuating states (**Fig. 12**). The criteria for γ_c^{macro} approximately coincides with the distortion of the characteristic Lissajous curves, as expected, since they are both controlled by the phase difference between stress and strain.

To verify that the simulation data used to determine both the microscopic and macroscopic criteria was reliable and reproducible, repeated simulations were run for selected volume fractions (see Appendix B).

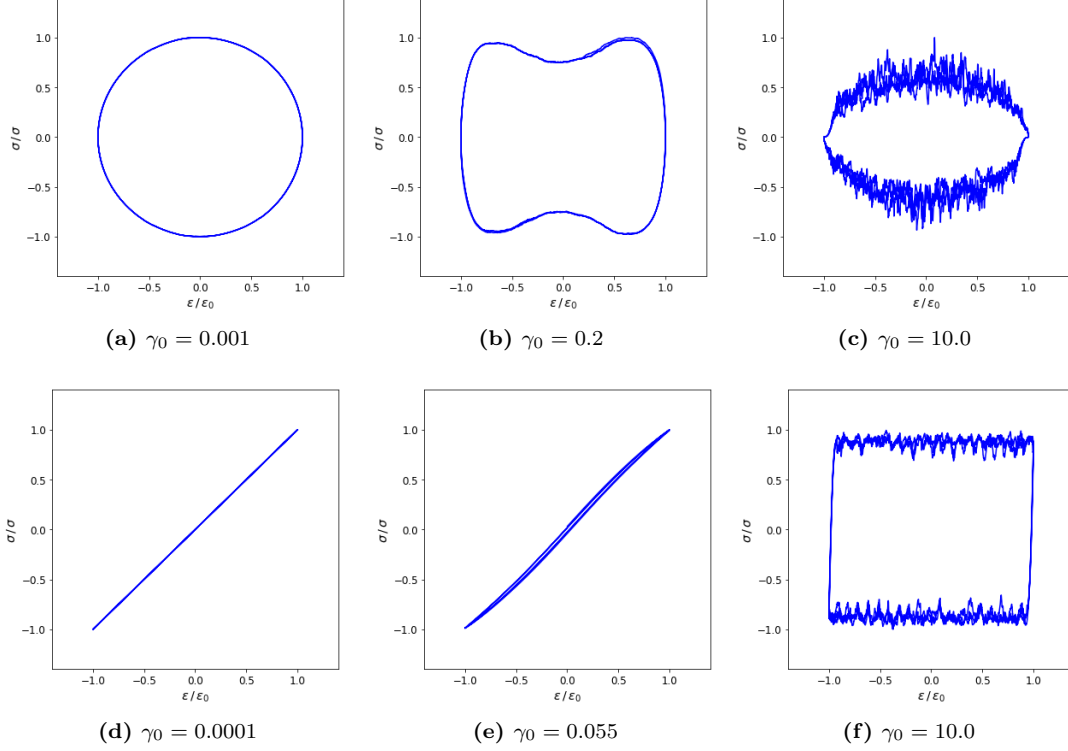


Figure 12: Typical stress-strain Lissajous figures for **(a-c)** concentrations below jamming ($\phi = 0.55$) and **(d-f)** above jamming ($\phi = 0.70$), with strain amplitude (γ_0) increasing from left to right. Examples of absorbing states below and above the jamming point are shown in **(a)** and **(d)**, respectively. The characteristic Lissajous curves become distorted at the transition point, shown in **(b)** and **(e)**, and are truly irreversible in **(c)** and **(f)**.

3.4 Phase diagram

Plotting the critical strain amplitudes (γ_c^{micro} and γ_c^{macro}) against volume fraction generates a phase diagram that indicates regions in which absorbing states can and cannot be formed (**Fig. 13**). It is difficult to determine the precise point at which the slope begins to change significantly on the various figures used to estimate γ_c^{micro} and γ_c^{macro} . Uncertainties in both critical strain amplitudes are estimated from the precision with which discrete values of γ_0 were sampled, as illustrated in **Figs. 8** and **11**.

At low volume fractions (below the jamming transition), absorbing states of the kind described in Refs. [3] and [4] are observed for low strain amplitudes. The concentration at which it is not possible to form an absorbing state, even for infinitesimally small γ_0 , is identified as the critical jamming volume fraction ϕ_c . Close

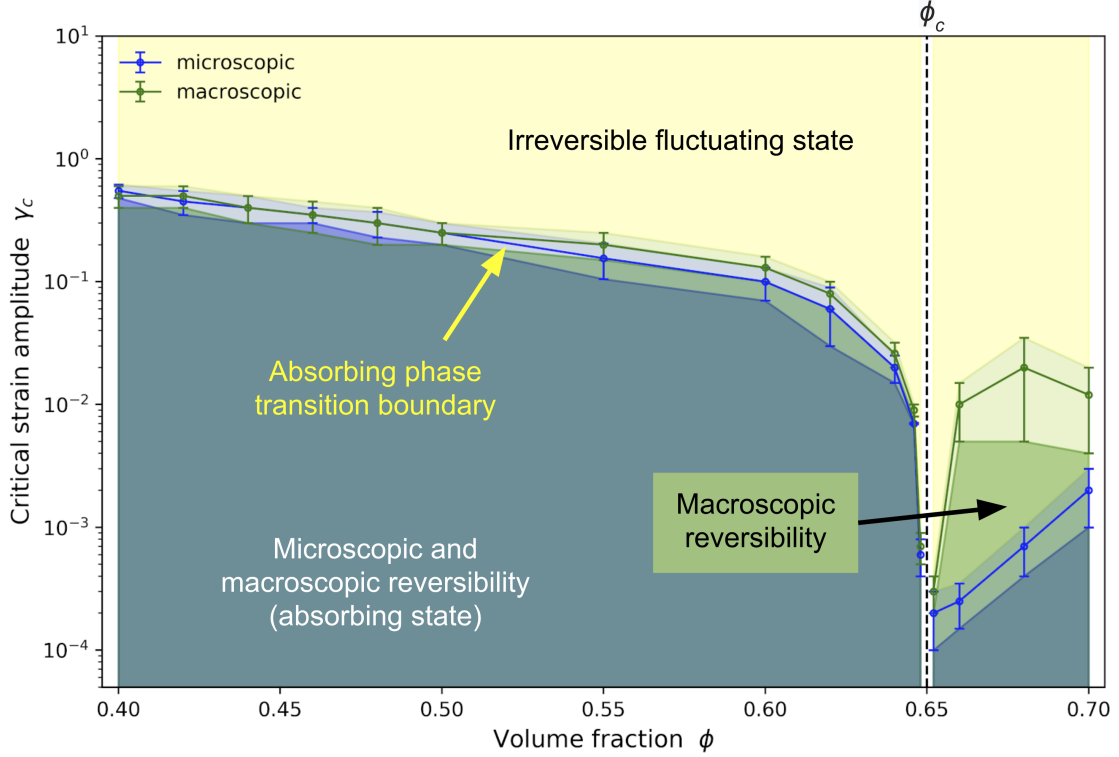


Figure 13: Phase diagram showing the boundary between regions in which absorbing states can and cannot be formed. The two phase boundaries shown correspond to the values of γ_c^{micro} and γ_c^{macro} as a function of volume fraction. The phase space containing irreversible fluctuating states is shaded in pale yellow. Underneath each boundary, states possess either microscopic or macroscopic reversibility. These areas are shaded in pale blue and green, respectively, with the regions that display both types of reversibility shaded in darker blue-green. Within the respective uncertainties of each boundary, the shading is fainter. The critical jamming concentration (ϕ_c), at which no absorbing states can be formed, even for infinitesimally small strain amplitudes, is indicated.

to the jamming point, γ_c^{micro} and γ_c^{macro} drop several orders of magnitude over a small concentration range. There is convincing evidence that absorbing states can be formed at $\phi = 0.646$ and $\phi = 0.654$, but results are inconclusive for $0.646 < \phi < 0.654$, placing upper and lower bounds on ϕ_c . The critical volume fraction, is therefore estimated to be $\phi_c = 0.650 \pm 0.004$. As the ϕ is increased beyond the jamming transition, γ_c^{micro} and γ_c^{macro} begin to increase and absorbing states of the kind described in Ref. [7] are observed at low strain amplitudes. The value of ϕ_c obtained is broadly consistent with other values in the literature [20, 21]. However, the precise value of ϕ_c varies depending on the exact properties of each system, such as the polydispersity and compression rate [22], so it is difficult to make a direct comparison.

Since the phase transition affects multiple aspects of the system's behaviour, we would expect to observe associated changes in the measured quantities at the same strain amplitude. There is a fairly good agreement between γ_c^{micro} and γ_c^{macro} for dilute systems at concentrations below the jamming point. However, above the jamming point, there is substantial disagreement between the two reversibility criteria – the signature depends strongly on how it is measured. Perhaps this complication is one of the reasons why there is so much debate about the nature of jamming and yielding of jammed materials.

It would be beneficial to develop more robust transition criteria, allowing more accurate identification of absorbing states. Ideally this would take the form of a universal criterion that can be applied to both types of absorbing states at concentrations above and below ϕ_c . However, achieving this may require a significantly different approach, such as considering the emergence of hyperuniform density fluctuations in the vicinity of the transition.

3.5 Hyperuniformity

Hyperuniform systems are amorphous states of matter that suppress large-scale density fluctuations in a similar way that crystals do, yet are isotropic with no Bragg peak like liquids or glasses [23]. For a system in d -dimensions, if the number of particles contained in a region of volume L^d is sampled at random locations throughout the system, the variance of density fluctuations takes the form $\sigma_\rho^2(L) \equiv \langle \rho^2(L) \rangle - \langle \rho(L) \rangle^2 \propto L^{-\lambda}$. For randomly distributed particles, these density fluctuations decay with exponent $\lambda = d$. If density fluctuations decay faster than this ($\lambda > d$), then the system is said to be hyperuniform, with crystalline systems achieving the maximum value of $\lambda = d + 1$.

It has been shown [24, 25, 26] for one and two-dimensional systems that a phase transition to an absorbing state is characterised by hyperuniform density fluctuations. Hexner & Levine [25] found that an absorbing state in two-dimensions is hyperuniform up to a correlation length ξ , which diverges at the critical strain amplitude for a given area fraction. Over small length scales $L \ll \xi$, density fluctuations decay with exponent $\lambda \approx 2.45 \equiv d + 0.45$; the exponent deviates from this value as L is increased, before reaching $\lambda = 2 \equiv d$ at $L = \xi$. By considering density fluctuations as a function of L for our more complex three-dimensional system, it may be possible to extract different correlation lengths ξ for each strain amplitude, as demonstrated in **Fig. 14a**. Plotting ξ as a function of γ_0 , one would hope to see a divergence in ξ at γ_c (**Fig. 14b**). If this divergence is observable for volume fractions below and above the jamming point, it could provide a way to unify absorbing state transitions in both regimes. However, the correlation length can become as large as $\mathcal{O}(10^2)$ particle diameters, so it would be impracticable to perform numerical simulations in three-dimensions without a powerful supercomputer.

4 Conclusions

Two types of absorbing states, were observed at concentrations above and below the critical volume fraction. The first type is analogous to those described in Refs. [3, 4, 5] and is formed in a viscous regime where

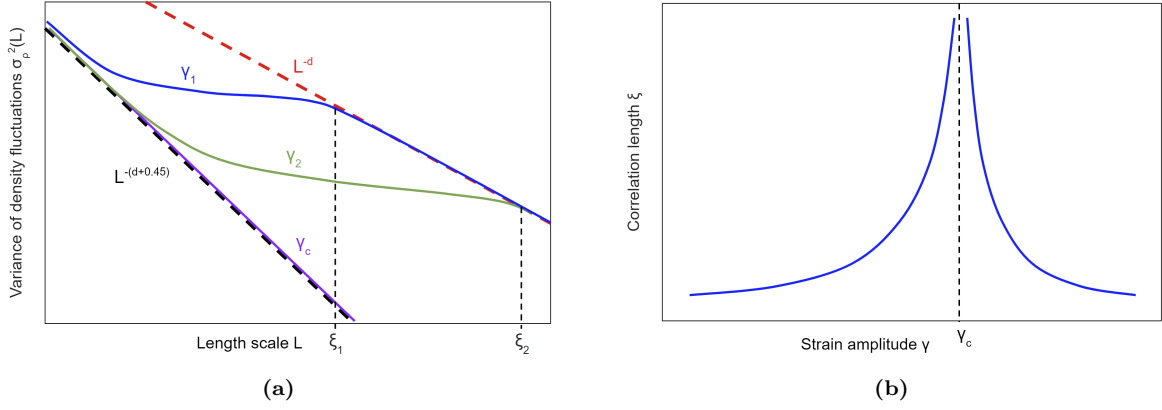


Figure 14: (a) A sketch showing approximately how we might expect to see the variance of density fluctuations ($\sigma_\rho^2(L)$) vary as a function of the length scale L over which they are considered for a d -dimensional system sheared at increasing strain amplitudes ($\gamma_1 < \gamma_2 < \gamma_c$). The red dotted line (L^{-d}) indicates the boundary for hyperuniformity. The system is hyperuniform up to a correlation length ξ , at which point $\sigma_\rho^2(L)$ meets the line L^{-d} . At the critical strain amplitude (γ_c), $\sigma_\rho^2(L)$ never reaches the line. (b) A sketch showing how the correlation length ξ might diverge at γ_c .

hydrodynamics dominates and the equations of motion are time-reversible. The second type is similar to that from Ref. [7] and is formed in a contact force dominant regime, where the route to reversibility is less obvious. The equations of motion are irreversible, but the system is able to self-organise into an absorbing state in which particles return to the same position each shear cycle.

The non-equilibrium phase transition that occurs was characterised by considering microscopic and macroscopic reversibility, and a strong dependence on the strain amplitude with which suspensions are sheared was found. There is good agreement between the both types of reversibility for dilute concentrations ($\phi < \phi_c$), but not for high concentrations ($\phi > \phi_c$); this inconsistency may offer some insight into why there are so many conflicting views on the nature of jamming and yielding of jammed materials. The jamming point, at which absorbing states cannot be formed, even for infinitesimally small strain amplitudes, was identified as $\phi_c = 0.650 \pm 0.004$, which is broadly consistent with values obtained in other studies [20, 21].

If I had more time, I would have liked to perform more simulations to obtain a more precise phase boundary and place tighter bounds on ϕ_c . To fully explore systems very close to the transition, where the time to reach an absorbing state diverges, simulations need to be extended for much longer. More importantly, future work should focus on finding a robust universal criterion that describes absorbing state transitions both below and above the jamming point. Considering hyperuniform density fluctuations and the divergence of the correlation length ξ could offer a potential solution. If so, it would be a significant step towards unifying the behaviour in two types of absorbing state that appear to be due to very different phenomena, and could offer further insight into the underlying mechanism behind absorbing-state transitions in granular suspensions.

Appendix A Scalar resistances

The scalar resistance matrix elements in the expressions for the hydrodynamic forces and torques in Section 2.1 are (for $\beta = a_2/a_1$) given by [11]:

$$X_A^{11} = 6\pi a_1 \left(\frac{2\beta^2}{(1+\beta)^3} \frac{1}{\xi} + \frac{\beta(1+7\beta+\beta^2)}{5(1+\beta)^3} \ln \left(\frac{1}{\xi} \right) \right) \quad (10)$$

$$Y_A^{11} = 6\pi a_1 \left(\frac{4\beta(2+\beta+2\beta^2)}{15(1+\beta)^3} \ln \left(\frac{1}{\xi} \right) \right) \quad (11)$$

$$Y_B^{11} = -4\pi a_1^2 \left(\frac{\beta(4+\beta)}{5(1+\beta)^2} \ln \left(\frac{1}{\xi} \right) \right) \quad (12)$$

$$Y_B^{21} = -4\pi a_2^2 \left(\frac{\beta^{-1}(4+\beta^{-1})}{5(1+\beta^{-1})^2} \ln \left(\frac{1}{\xi} \right) \right) \quad (13)$$

$$Y_C^{11} = 8\pi a_1^3 \left(\frac{2\beta}{5(1+\beta)} \ln \left(\frac{1}{\xi} \right) \right) \quad (14)$$

$$Y_C^{12} = 8\pi a_1^3 \left(\frac{\beta}{10(1+\beta)} \ln \left(\frac{1}{\xi} \right) \right) \quad (15)$$

Appendix B Repeated simulations

For the majority of points in strain amplitude-concentration phase space, only a single simulation was run due to limited CPU time. However, to test for reliability, different initial configurations of particles were generated, each using a different random seed. Repeated simulations were then carried out across a range of strain amplitudes for concentrations above (**Fig. 15a**) and below (**Fig. 15b**) the critical volume fraction. There is fairly good consistency between different realisations, and taking an ensemble average gives standard errors of the mean that are sufficiently small to be deemed negligible. With more time, I would ideally run more extensive repeated simulations over a wider range of concentrations.

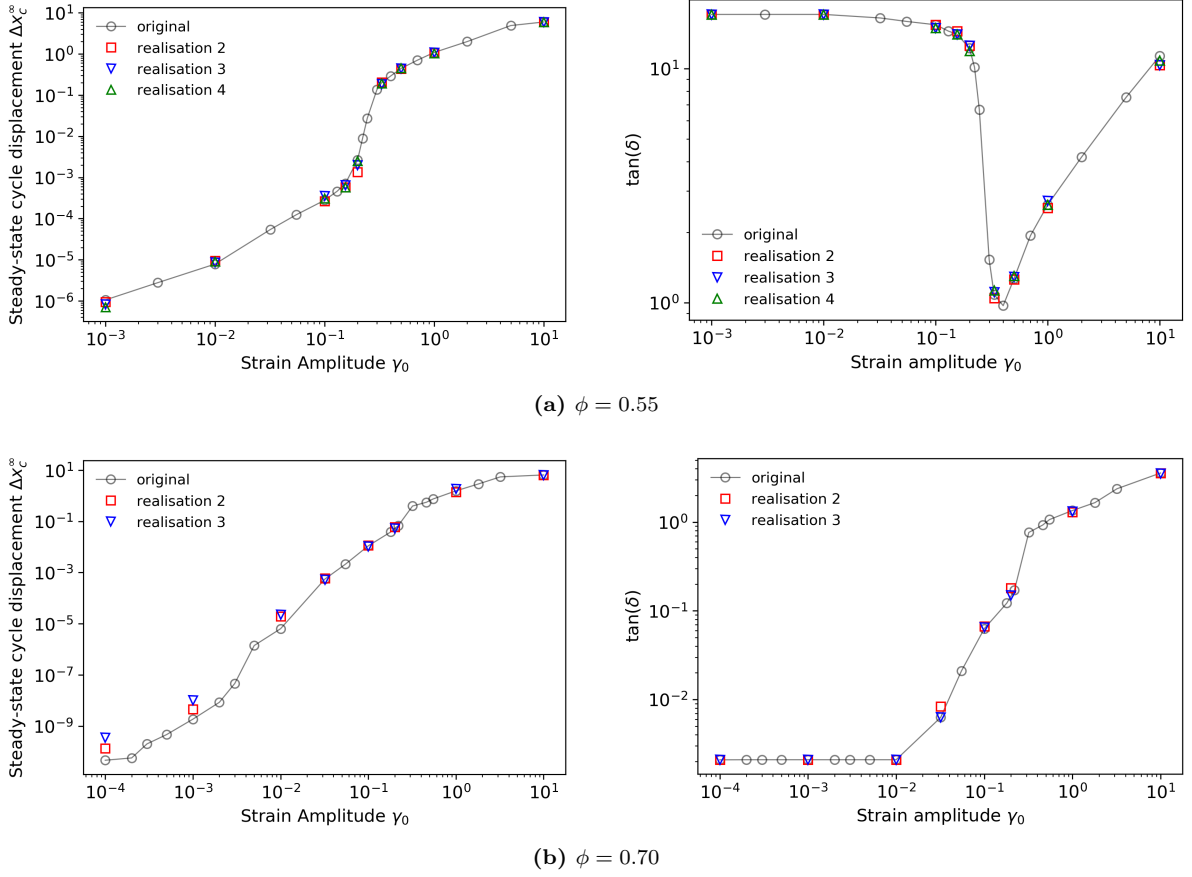


Figure 15: A comparison of repeated simulations to the original realisation for (a) $\phi = 0.55$ and (b) $\phi = 0.70$, where different realisations were generated using different random number seeds. The left hand plots show the steady-state cycle displacement (Δx_c^∞) as a function of strain amplitude (γ_0), while the right hand plots show the phase angle $\tan(\delta)$ between stress and strain as a function of γ_0 .

References

- [1] Hinrichsen H (2000) Non-equilibrium critical phenomena and phase transitions into absorbing states. *Advances in Physics* 49(7):815–958.
- [2] Benbow J, Bridgwater J (1993) *Paste flow and extrusion*. (Clarendon Press, Oxford).
- [3] Pine DJ, Gollub JP, Brady JF, Leshansky AM (2005) Chaos and threshold for irreversibility in sheared suspensions. *Nature* 438:997–1000.
- [4] Cort   L, Chaikin PM, Gollub JP, Pine DJ (2008) Random organization in periodically driven systems. *Nature Physics* 4:420–424.
- [5] Pham P, Butler JE, Metzger B (2016) Origin of critical strain amplitude in periodically sheared suspensions. *Physical Review Fluids* 1(2):022201.
- [6] Biroli G (2007) A new kind of phase transition? *Nature Physics* 3:222.

- [7] Royer JR, Chaikin PM (2015) Precisely cyclic sand: Self-organization of periodically sheared frictional grains. *Proceedings of the National Academy of Sciences* 112(1):49–53.
- [8] Cheal O, Ness C (2018) Rheology of dense granular suspensions under extensional flow. *Journal of Rheology* 62(2):501–512.
- [9] Ball R, Melrose J (1997) A simulation technique for many spheres in quasi-static motion under frame-invariant pair drag and Brownian forces. *Physica A: Statistical Mechanics and its Applications* 247(1-4):444–472.
- [10] Jeffrey DJ (1992) The calculation of the low Reynolds number resistance functions for two unequal spheres. *Physics of Fluids A: Fluid Dynamics* 4(1):16–29.
- [11] Kim S, Karrila S (1991) *Microhydrodynamics: Principles and selected applications*. (Butterworth-Heinemann, Boston).
- [12] Radhakrishnan R (2017) Derivation of lubrication forces for unequal spheres. <https://doi.org/10.5281/zenodo.1137305>.
- [13] Comtet J, et al. (2017) Pairwise frictional profile between particles determines discontinuous shear thickening transition in non-colloidal suspensions. *Nature communications* 8:15633.
- [14] Cundall PA, Strack ODL (1979) A discrete numerical model for granular assemblies. *Geotechnique* 29(1):47–65.
- [15] Plimpton S (1995) Fast parallel algorithms for short-range molecular dynamics. *J. Comp. Phys.* 117:1–19.
- [16] Chialvo S, Sun J, Sundaresan S (2012) Bridging the rheology of granular flows in three regimes. *Phys. Rev. E* 85(2):021305.
- [17] Ness C, Mari R, Cates ME (2018) Shaken and stirred: Random organization reduces viscosity and dissipation in granular suspensions. *Science Advances* 4(3). eaar3296.
- [18] Christopoulou C, Petekidis G, Erwin B, Cloitre M, Vlassopoulos D (2009) Ageing and yield behaviour in model soft colloidal glasses. *Philosophical Transactions of the Royal Society of London A: Mathematical, Physical and Engineering Sciences* 367(1909):5051–5071.
- [19] Denisov DV, et al. (2015) Sharp symmetry-change marks the mechanical failure transition of glasses. *Scientific Reports* 5:14359.

- [20] Zhang HP, Makse HA (2005) Jamming transition in emulsions and granular materials. *Phys. Rev. E* 72(1):011301.
- [21] Chialvo S, Sun J, Sundaresan S (2012) Bridging the rheology of granular flows in three regimes. *Phys. Rev. E* 85(2):021305.
- [22] Baranau V, Tallarek U (2014) Random-close packing limits for monodisperse and polydisperse hard spheres. *Soft Matter* 10(21):3826–3841.
- [23] Torquato S (2016) Hyperuniformity and its generalizations. *Phys. Rev. E* 94(2):022122.
- [24] Tjhung E, Berthier L (2015) Hyperuniform density fluctuations and diverging dynamic correlations in periodically driven colloidal suspensions. *Phys. Rev. Lett.* 114(14):148301.
- [25] Hexner D, Levine D (2015) Hyperuniformity of critical absorbing states. *Phys. Rev. Lett.* 114(11):110602.
- [26] Hexner D, Chaikin PM, Levine D (2017) Enhanced hyperuniformity from random reorganization. *Proceedings of the National Academy of Sciences* 114(17):4294–4299.